Physical Biology

PAPER

Role of combined cell membrane and wall mechanical properties regulated by polarity signals in cell budding

RECEIVED
30 April 2020

REVISED
12 August 2020

ACCEPTED FOR PUBLICATION
24 August 2020

PUBLISHED
15 October 2020

Kevin Tsai[1,2], Samuel Britton[1,2], Ali Nematbakhsh[1,2,3], Roya Zandi[4,2], Weitao Chen[1,2,*] and Mark Alber[1,2,*]

[1] Department of Mathematics, University of California, Riverside, CA, United States of America
[2] Interdisciplinary Center for Quantitative Modeling in Biology, University of California, Riverside, CA, United States of America
[3] Cornell Institute of Biotechnology, Cornell University, NY, United States of America
[4] Department of Physics and Astronomy, University of California, Riverside, CA, United States of America
[*] Authors to whom any correspondence should be addressed.

E-mail: malber@ucr.edu and weitaoc@ucr.edu

Keywords: asymmetric cell growth, three-dimensional modeling, particle model, protein polarization, yeast budding, computational biology, mechanistic model

Supplementary material for this article is available online

Abstract

Budding yeast, *Saccharomyces cerevisiae,* serves as a prime biological model to study mechanisms underlying asymmetric growth. Previous studies have shown that prior to bud emergence, polarization of a conserved small GTPase Cdc42 must be established on the cell membrane of a budding yeast. Additionally, such polarization contributes to the delivery of cell wall remodeling enzymes and hydrolase from cytosol through the membrane, to change the mechanical properties of the cell wall. This leads to the hypothesis that Cdc42 and its associated proteins at least indirectly regulate cell surface mechanical properties. However, how the surface mechanical properties in the emerging bud are changed and whether such change is important are not well understood. To test several hypothesised mechanisms, a novel three-dimensional coarse-grained particle-based model has been developed which describes inhomogeneous mechanical properties of the cell surface. Model simulations predict alternation of the levels of stretching and bending stiffness of the cell surface in the bud region by the polarized Cdc42 signals is essential for initiating bud formation. Model simulations also suggest that bud shape depends strongly on the distribution of the polarized signaling molecules while the neck width of the emerging bud is strongly impacted by the mechanical properties of the chitin and septin rings. Moreover, the temporal change of the bud mechanical properties is shown to affect the symmetry of the bud shape. The 3D model of asymmetric cell growth can also be used for studying viral budding and other vegetative reproduction processes performed via budding, as well as detailed studies of cell growth.

1. Introduction

In this paper, a three-dimensional model is introduced for studying asymmetric cell growth, a prominent reproductive process utilized in many organisms to generate cell diversity during development. It is also important in determining cell fate when, for example, stem cells divide for the purpose of proliferation or differentiation. The budding yeast *Saccharomyces cerevisiae* is a fungus that can reproduce via asymmetric growth and serves as a classic model to study the principles underlying this fundamental process [1–8]. Reproduction in the budding yeast, is a delicate process governed by a combination of dynamically changing biochemical signaling networks, turgor pressure, transport of subcellular organelles, and regulation of the mechanical properties of the yeast cell surface, consisting of cell wall, cell membrane and periplasm between them.

Structurally, the yeast cell wall is a dynamic network primarily composed of polysaccharides. The cell wall network is composed of 1, 3-β-glucan, 1, 6-β-glucan, and a relatively small amount of chitin proteins. Linkage between the 1, 3-β-glucan, 1, 6-β-glucan, and chitin proteins are established to maintain the structural integrity of the cell wall [9]. Beneath

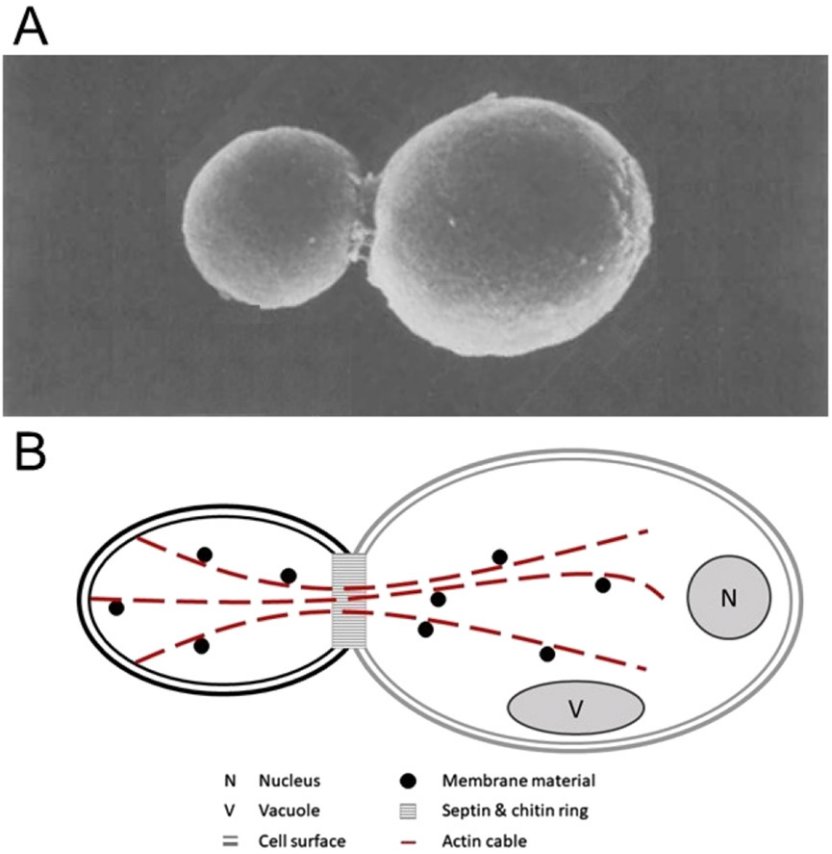

Figure 1. Experimental image (A) and representative diagram (B) of the yeast mother cell (right) and the developing bud (left) separated by the chitin and septin rings. (B) Cell wall (outer boundary) and membrane (inner boundary) are represented by two curves. Internal components of the mother cell include nucleus and vacuole. Actin cables (dashed red lines) polarize at the bud site and recruit new cell membrane/wall materials (black points). (Image A is reproduced with permission from Hanschke *et al* [10]).

the cell wall structure lies the cell membrane consisting of lipids and membrane-bound proteins similar to the membrane in animals. While the cell wall mechanically supports the cell integrity in response to forces from the environment and maintains cell shape, the cell membrane acts as the barrier to the free diffusion in the cytosol, provides binding sites for molecular signaling pathways involved in the biosynthesis of cellular components, and relays the environmental conditions to the cell interior via signaling transduction pathways to regulate the osmotic balance [11].

Yeast budding starts with a protrusion in the cell surface and results in cell division to form a daughter cell separated from the mother (figure 1(A)). A single bud is generated in one cell cycle. Notice that no nucleus is formed yet in the bud at the early stage (figure 1(B)) [12]. The location of the protrusion site, or the bud site, is determined by asymmetric distribution of Cdc42 and growth-associated proteins established before cell shape change, which is followed by a polarization of structural components including actin cables, septin, and myosin [13, 14]. These polarization events play an important role in budding. It has been shown experimentally that multiple concurrent protrusions during the budding process occur when the Cdc42 signaling pathway is impaired [15].

Shortly before the protrusion occurs, septins and chitins within the cell membrane and cell wall are assembled to form ring-like structures [16, 17] (figure 1). It has been shown that the septin rings and the chitin rings, located in the cell membrane and cell wall, respectively, have similar functionality in controlling the size of the budding neck via different mechanisms, and the synthases responsible for the assembly of these two rings are related [18]. Presence of the rings is essential. They colocalize and, along with the linkage between the chitin rings and 1,3-β-glucan, limit the expansion along the neck during budding. Moreover, these two rings, especially the septin rings, act as a diffusion barrier impacting bud morphogenesis [6, 19]. Meanwhile, actin cables polarize to direct the transport of secretory vesicles as well as new cell membrane and cell wall materials from the cytosol to the budding site. Several studies have suggested that mutants which have improper formation of the chitin and septin rings or polarized actin cables give rise to wide budding necks, which can be detrimental to the survival of the cell [20–22].

During the early stages of the budding process, the mother cell exhibits marginal change in size and the turgor pressure remains sufficiently constant in the rage of 0.1–1.0 MPa [23–25]. A recent study also

suggests that during the entire reproduction cycle, the turgor pressure remains at approximately 0.21 MPa [26]. While the turgor pressure acts as the driving force to generate a bulge on the cell surface, the cell wall of the bud region where Cdc42 polarizes is weakened by the secreted hydrolases and cell wall remodeling is promoted by the actin-mediated delivery of secretory vesicles [14]. This leads to degradation of the β-glucan network in the cell wall and at the same time the recruitment of new materials to the cell wall and cell membrane. While Cdc42 has not yet been reported to directly regulate the cell surface elasticity, its polarization leads to the correct polarization of the actin cables responsible for secretory vesicle and subcellular component delivery, which has been identified in [27]. On the other hand, Cdc42 has been shown to promote cell wall degradation during yeast mating by colocalization with Fus2p protein [28, 29], demonstrating its contribution on altering cell wall properties. Hence it is reasonable to assume that the cell surface mechanical properties are indirectly regulated, if not a direct regulation, and influenced by Cdc42 polarization and its downstream processes.

However, it is challenging to experimentally measure mechanical properties of the cell surface in actively growing cells. Recently, the elasticity of the cell wall was measured during the yeast budding process and it was found that stiffness of the bud was slightly higher than that of the mother cell, although the obtained value may depend on the timing of measurements and the highly curved surface [30]. This result is different from an earlier observation in which the cell wall at the budding site becomes less rigid prior to bud emergence [14, 31]. It, therefore, remains unclear whether the change in mechanical properties of the yeast cell surface is necessary for the bud emergence. Moreover, it is not known how the mechanical properties of the cell surface are regulated to form a bud with appropriate shape.

Multiple computational models have been developed to propose and test different mechanisms underlying the budding process such as the clathrin-mediated endocytosis [32, 33] and the wrapping of nanoparticles [34–36]. In Gompper *et al* [37–39], a tether-and-bead model was developed to study cell surfaces with fixed sizes and fluctuating topologies, where the cell surface was discretized by a triangulated mesh and a probabilistic re-meshing algorithm was introduced to represent cell growth. This model has been extended into a particle-based framework to study the effect of molecular turnover and the material exchange between the cell membrane and cytosol on the cell shape by incorporating a mesh-refinement algorithm [40] to facilitate the stability of the model in capturing local cell surface deformation.

On the other hand, several computational models have been developed to study morphogenesis based on a description of the entire inhomogeneous cell wall. For example, in a model for the mating yeast, cell wall was described as an inhomogeneous viscous fluid shell and coupled with the cell wall integrity signaling pathway, which governs the wall synthesis and controls its stiffness, to study the coordination of mechanical feedback in cell wall expansion and assembly in mating yeast [41]. Similar approaches have been applied to study the tip growth of the pollen tube in plants [42]. In [30], the interplay between the turgor pressure and the elasto-plasticity of the cell wall during yeast budding was investigated by using a single-cell growth model. Mother cell and bud are represented as two separate spheres with identical wall elasticity but different levels of plasticity. Growth is described by the dynamics of cell radius, which is impacted by different levels of wall plasticity and fluctuating turgor pressure. Simulation results suggest that the bud must be significantly more exposed to plastic expansion compared to the mother cell in order for proper bud formation to take place.

In this paper, a novel 3D coarse-grained particle-based model is described and used to examine the impact of changing mechanical properties of combined cell membrane and cell wall (called cell surface hereafter) on the bud formation in yeast cells. Specifically, model simulations show how local cell surface growth and deformation in an early bud formation, controlled by experimentally observed polarized distribution of Cdc42, impacts the global deformation of the cell surface. Model parameters were calibrated to resemble the Young's modulus of the cell wall measured in experiments [43]. The model assumes that the turgor pressure remains constant throughout the early stages of the budding process which we focus on in this paper. Additionally, the model assumes ratios of stretching to bending modulus of the bud and mother cell to be different from each other, which is based on the experimentally observed presence of wall-degrading enzymes at the bud site. (Description of the terminology used in the paper is provided in the table S5 (https://stacks.iop.org/PB/17/065011/mmedia)).

Model simulation results indicate that increased dimensionless stretching to bending stiffness ratio, Föppl–von Kármán number, within the bud region at the early stage can influence bud emergence and the resulting bud shape. The reduction in bending stiffness, leading to a higher Föppl–von Kármán number, is necessary to drive bud emergence, and an unweakened or stiffer budding region leads to bud inhibition in our simulation. Chitin and septin rings were shown computationally to impact the neck shape without changing the bud sphericity, as well as the requirement on the Föppl–von Kármán number characterizing bud emergence. By varying the distribution of the polarized mechanical regulator, we demonstrate that reduced polarized signal distribution may lead

to asymmetric bud formation. Moreover, by assuming that the mechanical properties at the bud site can recover in time to the same level as those of the mother cell, we show that buds can acquire a symmetric shape similar to those observed in experiments. The new model can be extended to study the impact of dynamical changes of molecular distributions in yeast budding, as well as viral budding and other vegetative reproduction processes performed via budding.

2. Methods

2.1. General model description

Yeast mother cells can be either egg-shaped, elliptical, or spherical [44]. While the size of a yeast cell varies depending on the cell type, for simplicity we assume that mother cell initially is a sphere of radius of 2.0 μm [45]. The sphere, representing the cell wall and membrane, is discretized into a triangulated mesh. The triangulated surface is a simplified representation of the elastic network of the yeast cell surface. The nodes are connected by linear springs in each triangle to capture the in-plane elasticity, whereas the bending springs are applied to triangles sharing a common edge to model the out-of-plane elasticity (figure 2) [46, 47].

This discretization allows calibration of the model elasticity using experimental data by probing the elastic response under stress (section 2.5). We also assume that the bud site has been predetermined and Cdc42 becomes polarized to regulate the elasticity at the bud site.

The bud site is enclosed by the chitin and septin rings which are approximately 1μm in diameter [48]. The size of the rings remains unchanged throughout the budding process. While the mechanical role of the rings has yet to be confirmed experimentally, the lack of the change of the rings and bud neck size, indicates a constraining effect. In the model, the bud neck is represented by using a set of linear springs with a stiffness an order of magnitude higher than the one used to model the surface of the mother resulting in a rigid rings type behavior (equation (2)). Furthermore, the rings act as a demarcation separating bud site and mother cell (figure 2) [48, 49]. Distinct mechanical properties are assigned to the bud surface under the influence of wall degrading enzymes and to the mother cell surface. Previously developed remeshing techniques [38, 40, 50, 51] are utilized in the model to capture the structural response to osmotic pressure [52, 53].

Computational implementation. The iFEM [54], an MATLAB software package, was used to generate the initial mesh configuration. The density of the triangulated mesh can be changed according to the requirement of the resolution of the modeling system. In all simulations included in this paper without specification, the number of triangles used for the mother cell at the beginning of the simulation is 1280, and out of them 24 triangles belong to the budding region. For detailed description of the numerical simulation process, see section 2.6.

2.2. Equations of motion

Motion of each node i from the model representation of the cell surface is described by the following equation:

$$c\dot{x}_i(t) = -\nabla_{x_i}(E_{\text{total}}) + F_{\text{turgor},x_i}, \tag{1}$$

where c is the friction coefficient depicting the viscosity of the cell surface, ∇_{x_i} represents the gradient with respect to the ith node position, E_{total} represents the total potential energy used to model the mechanical properties of the surface of the cell and F_{turgor} is the force derived from the force-stress relationship originating from the constant turgor pressure acting on the cell surface. The numerical integration for solving this differential equation is performed using the standard Euler's method. (More details are provided in sections 2.3–2.6).

We define the total potential energies used to model the cell surface: $E_{\text{total}} = E_{\text{linear}} + E_{\text{area}} + E_{\text{bend}} + E_{\text{volex}}$. Here, E_{linear} is the linear potential between connected nodes and E_{volex} is volume exclusion property imposed between nodes that are not connected by an edge, modeling the self-avoiding property preventing cell-cell intersection. E_{area} and E_{bend} represent area and bending potentials yielding forces that control the area expansion resistance of each individual triangular element and level of bending between triangular elements. Due to the micron scale of the yeast cell and fluid environment required for yeast reproduction, the surrounding microenvironment acts as an overdamping media. We therefore assume that the cell in the model is in the overdamped regime where the inertia force is negligible [40, 55].

Notice that each mechanical potential comprising E_{total} is chosen to represent cell surface elasticity, shape maintenance, and surface incompressibility, as described in section 2.3. While the choice of the components of energy potential function is not unique, we believe that our results are inline with other forms of energy potential function which have previously been used to describe the cell surface [40, 56–58]. Potentials in the model were calibrated via simulated cell stretching tests, and adjusted to match the experimental atomic force microscopy (AFM) data, as described in section 2.5.

2.3. Interaction potentials

We assume linear stiffness of the cell surface under low stress and use the internodal potential for nodes connected via an edge in the following form:

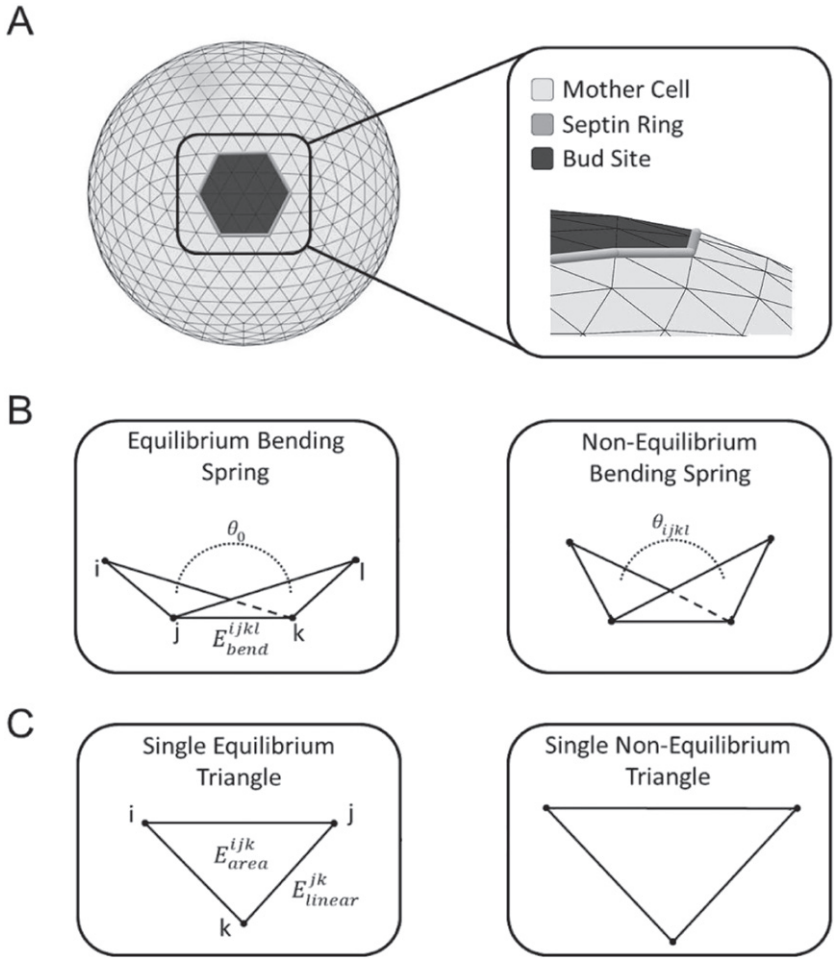

Figure 2. Schematic diagram of components comprising the *in silico* yeast cell model. (A) Initial simulated mother cell representation including predetermined bud region (dark gray), combined chitin and septin rings (gray tubes), and mother cell surface (light gray). (B) and (C) Individual model spring elements are shown at equilibrium (left) and non-equilibrium (right).

$$E_{\text{linear}} = \sum_{i,j \in B(\text{cell})} \left(\frac{k_s}{2}\right)\left(L_{ij} - L_0\right)^2, \qquad (2)$$

where k_s is the linear spring coefficient, L_{ij} is the length of the spring connecting node i and node j, and L_0 is the equilibrium length of the bond. The sum is taken over all edges of the mesh, denoted by $B(\text{cell})$. As described in section 2.1, interactions between nodes of edges separating the budding region and the remainder of the mother cell are also represented by a similar internodal potential but the coefficient is scaled with ${L_0}^2$. Namely, the sum of the energy potentials of the form ${E_{\text{linear}}}^{\text{ring}} = ({k_s}^{\text{ring}}/(2{L_0}^2))(L_{ij} - L_0)^2$ models the stiffness of segments of the chitin and septin rings on the mesh.

Following previous works [40, 56], the local area expansion resistance of each individual triangular facet is represented using a harmonic potential:

$$E_{\text{area}} = \sum_{T_{ijk} \in T(\text{cell})} \left(\frac{k_a}{2A_0}\right)\left(A_{ijk} - A_0\right)^2, \qquad (3)$$

where k_a is the area expansion resistance coefficient, A_{ijk} is the current area of the triangle T_{ijk}, and A_0 is the equilibrium triangle area. The sum is taken over all triangular elements $T(\text{cell})$.

To maintain the spherical shape, we adopt the approach that utilizes the angle-bending potentials between neighboring triangles that share a common edge to enforce cell surface curvature. In particular, we apply the method proposed in [59]. The explicit relationship between the equilibrium angle and the radius of curvature is $\sin(\theta_0/2) = (12R_0^2/L_0^2 - 3)^{-\frac{1}{2}}$ where θ_0 is the equilibrium dihedral angle between unit normal vectors of edge-sharing triangles, R_0 is the radius of curvature, and L_0 is the equilibrium edge length of the triangle [60]. Hence, the bending behavior is determined by the cosine bending potential based on the unit normal vectors of edge-sharing triangles:

$$E_{\text{bend}} = \sum_{b_{ij} \in B(\text{cell})} k_b(1 - \cos(\theta_{ij} - \theta_0)), \qquad (4)$$

where k_b is the bending coefficient, θ_{ij} is the current dihedral angle between the unit normal vectors of two triangles sharing edge b_{ij}, and θ_0 is the equilibrium dihedral angle. The sum is taken over all edges over the surface $B(\text{cell})$.

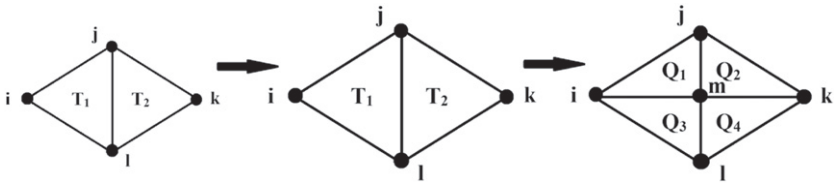

Figure 3. The growth (expansion) algorithm. Initial pair of triangles with a common edge (left) expands under stress (middle) resulting in a triangulation (right) after addition of a new node and new edges. This algorithm is used if the average area of T_1 and T_2 exceeds the critical value of γ.

Volume exclusion constraints, E_{volex}, are introduced to incorporate the self-avoiding property of different domains of the cell surface avoiding each other. Several models, whether with or without defining an absolute minimum distance between cell surface nodes, have employed compression-resistance potential [40, 56]. The self-avoiding property is also necessary to maintain the numerical stability and cell surface topology to avoid concavity. We apply the standard Morse potential to enforce the self-avoiding property for non-connected nodes:

$$E_{\text{volex}} = \sum_{i,j} D(1 - \exp(-a(L_{ij}^{\text{rep}} - L_0^{\text{rep}})))^2,$$
$$L_{ij}^{\text{rep}} \leqslant L_0^{\text{rep}},\ j \notin N(i). \tag{5}$$

Here D represents the well depth of the Morse potential with width a. L_{ij}^{rep} represents the distance between any two non-connecting nodes, L_0^{rep} is the optimal distance between any two non-connecting nodes, and $N(i)$ is the collection of nodes connected to a given node i. Parameter values and the calibration are described in section 2.5.

2.4. Modeling cell growth

During the budding process, the yeast cell undergoes a local deformation with a narrow neck formation and cell surface material insertion to the bud site. To capture both geometric change and the expansion of the surface, we incorporate a re-meshing technique into the model.

To alter the edge-connectivity in the current mesh, which is to obtain a new geometry favoring bud formation, we employ the Monte Carlo edge re-connectivity algorithm. The Monte Carlo simulation for edge re-connectivity (also termed bond-flip) is a well-established approach and has been shown to effectively capture the topological change which is essential in surface deformation and protein folding [38, 50, 51]. The edge re-connectivity is determined probabilistically via energy-based comparison between the pre- and post-flip of edges in the existing mesh.

In order to describe an increase of the area of the bud, we define a quantity called strain associated with the area expansion

$$\gamma = \frac{A_{ijk} - A_0}{A_0}, \tag{6}$$

where A_0 is the equilibrium area and A_{ijk} is the current area of the triangle. During the simulation, if the value of γ exceeds a critical value, $\overline{\gamma}$, then new triangles are introduced into the system following the approach from [40]. Physically, this corresponds to the instance when new material insertion to the cell surface from the bulk is more energetically favorable. Biologically, it represents the response of a cell to excessive mechanical stress. Specifically, if the relative change in average area of two adjacent triangles, T_1 and T_2, is larger than $\overline{\gamma}$, a new node, m, is introduced at the center of the shared edge (figure 3). T_1 and T_2 are subsequently divided using the newly placed node, thereby creating four new triangles, $Q_1, \ldots, Q_4$.

To utilize this form of growth algorithm, we check this growth condition over every pair of triangles sharing a common edge inside the budding region, and call this sweeping process as one growth step.

We assume that the turgor pressure is constant at the initiation of the budding stage we model, and the surface deformation at every step is small. For each triangle in the model, the force due to the turgor pressure acting on the node i is as follows,

$$F_{\text{turgor},x_i} = \sum_{T_{ijk} \in T(i)} \frac{1}{3} A_{ijk} P \hat{n}, \tag{7}$$

where A_{ijk} is the current area of the triangle T_{ijk}, P is the constant turgor pressure and $\hat{n}$ is the outward unit normal vector of the triangle. The sum is taken over triangles containing node i, denoted by $T(i)$, in order to obtain the consistent force due to the turgor pressure applied to the overall cell surface [26].

2.5. Model calibration

In experiments, whole cell compression [61] and probing via AFM [43] are common approaches to measure the mechanical properties of a single cell including the stretching modulus and bending modulus on the cell surface.

While both methods have been applied to identify the elasticity of the yeast cell wall, the reported values differ from each other by up to two orders of magnitude. The model described in this paper was calibrated by using the measurement of the cell surface elasticity obtained by AFM in [43]. In

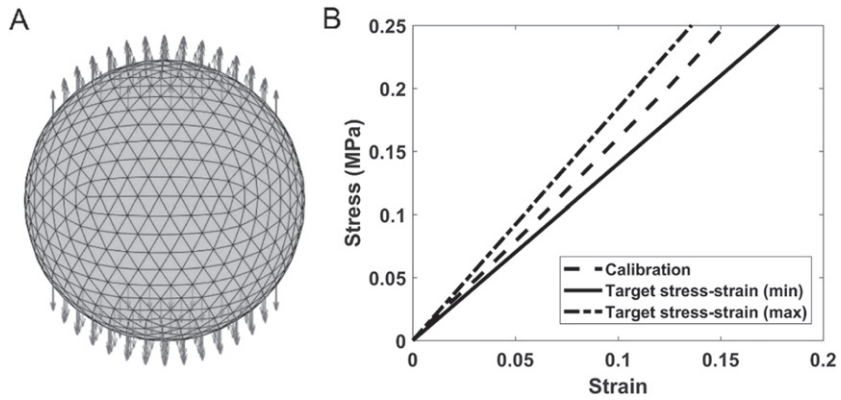

Figure 4. Calibration of the mechanical model for a single yeast cell without budding. (A) Forces of opposite directions are applied to detect the elasticity properties of the cell based on a chosen parameter set. (B) The stress-strain ratio (dashed line) using parameters $k_s = 2.0$, $k_a = 2.0$ and $k_b = 0.5$. The min and max of the target stress-strain ratio is obtained from Dague *et al* [43].

this experiment, a nanoindentation on the cell wall was created and the modulus of elasticity was identified as 1.62 ± 0.22 MPa for a yeast cell prior to bud emergence.

During calibration, linear stiffness, bending stiffness and area expansion resistance coefficient are calculated after applying forces of the same magnitude in the opposite directions to a single cell having initially a spherical shape (figure 4(A)). Re-meshing is not allowed in this simulation by assuming that the cell is not actively growing at this step of the algorithm. To reduce the sample size required in exploring the parameter space, we apply Latin hypercube sampling (LHS) to generate a sufficient amount of samples distributed over the wide range [62, 63]. Model simulations with the parameter set $k_s = 2.0, k_a = 2.0, k_b = 0.5$ obtained as a result of calibration, produced an elastic response which results in the correct material behavior of the cell surface, plotted in a dashed line, falling within the experimental data shown as solid lines in figure 4(B). We use this parameter set as the wild type condition for the mother cell in the following sections unless specified otherwise. Parameter values used in the model simulations, including the equilibrium edge length and dihedral angle, are provided in the supplemental information (table S2).

2.6. Numerical implementation of the model

Following the modeling construction described in section 2.1, basic data structures such as the x, y, z-coordinates of each node and associated nodes for each triangle must be generated. Advanced data structures of edge-sharing triangles, connectivity between nodes, and associated edges for each triangle are necessary for inefficient simulation. These data structures are generated via both built-in functions in iFEM and in-house functions written by us. The positional update of each node is described in section 2.2.

During the calibration of model parameters using the LHS, we divide the parameter value range into three uniform subspaces which in total give us 27 subspaces. We draw six sample points abiding the LHS requirements. Our initial ranges are $[0.0, 40.0]$, $[0.0, 20.0]$, and $[0.0, 40.0]$ for k_s, k_b, k_a, respectively. The sampling undergoes a total of six rounds of LHS, narrowing down the parameter space in each round, to reach a parameter set that grants similar elasticity from the experimental data. In each round, the subspace with the closest match to the experimental data is again divided into four subspaces. Fine tuning of the parameter set is carried out manually when the parameter set found using the sampling technique produces a fair estimate.

Numerical model simulations involve cycles of relaxation of the system to reach a local minimum of the total energy and growth cycles of the cell surface. During a relaxation cycle, a maximal number of $N_{\text{relaxation}} = 200$ steps, which is sufficient to reach the minimal energy, are performed with each relaxation step size $\Delta t = 0.001$. Immediately following each relaxation cycle, the Monte Carlo based edge reconnectivity algorithm (see section 2.4) is performed [40, 51, 56], to explore a sufficiently large number of different edges connecting cell surface nodes prior to implementing the stochastic cell surface growth algorithm. A growth cycle is triggered after N times of edge re-connectivity algorithm implementation, where N is chosen to be 100 in our model. The numerical simulation is terminated when the total volume of the cell reaches some target value or the maximum number of steps (1.6×10^7 steps) is reached. Note that the choices of $N_{\text{relaxation}}$, N, and Δt are case dependent and adjustable in different applications to achieve both numerical stability and computational efficiency.

The cell volume is calculated as $V = \frac{1}{6}\left|\left(\sum_j (P_{0,j} \cdot N_j)\left|N_j \cdot \{\sum_k P_{k,j} \times P_{k+1,j}\}\right|\right)\right|$, where $P_{*,j}$ is the vertices associated with jth triangle, and $N_j = \{(P_{1,j} - P_{0,j})$

$\times (P_{2,j} - P_{0,j})\}/\left|(P_{1,j} - P_{0,j}) \times (P_{2,j} - P_{0,j})\right|$ [64]. This formula provides the total volume using the absolute value of the sum of volumes which can be positive or negative. The sign indicates whether the triangular pyramid is initiated within the interior or exterior of the surface. The total volume is calculated by summing up volumes of all the triangular pyramids created by connecting each triangle on the mesh to the center of the mother cell.

3. Results

Prior to budding, Cdc42, small molecule GTPase, forms a cluster at a predetermined cortical site and orients actin cables toward the cluster. These cables then direct delivery of more Cdc42 as well as new cell membrane and cell wall materials using secretory vesicles to the cluster. This establishes a positive feedback loop to help establish the Cdc42 polarization and regulates cell surface mechanics at the bud site to prepare for budding [14, 27, 65].

The 3D computational model described in the previous section is used to determine whether changes in the cell surface elasticity at the bud site is required for bud formation and how these changes impact bud shape. In particular, we tested time-independent, spatial-dependent, and time-dependent changes in the mechanical properties, based on the spatiotemporal distribution of Cdc42 observed at different stages in experiments.

To model the impact of Cdc42 on the bud site enclosed by chitin and septin rings, each coefficient k_* defined in equations (2)–(4), is multiplied by a weight constant α_* varied between 0.0 and 1.0 (figure 2). α_s, α_b, and α_a, denote the weights for the stretching coefficient, bending coefficient, and the area expansion resistance coefficient, respectively.

In each simulation, the maximum number of iterative steps is $N = 1.6 \times 10^7$ with a total number of 800 growth steps. Since the focus of the paper is on the early stage of the budding process, a simulation is terminated when all growth steps are performed or cell volume reaches 1.5 of the initial volume. All simulations described in this section used the turgor pressure $P = 0.2$ MPa. A snapshot of a typical bud emergence simulation is shown in figure 5.

3.1. Role of elasticity of cell surface in yeast budding

In this section we keep the weight constants throughout the bud site in time by assuming that polarization of Cdc42 is established before the mechanical properties of the bud are changed. First, the dimensionless ratio of stretching to bending moduli and the critical value $\overline{\gamma}$ required for bud emergence are determined. Next, their impact on the shape after budding occurs is studied.

3.1.1. Dimensionless ratio of stretching to bending stiffness

In the theory of elasticity, the ratio between the stretching and bending moduli determines the physical property of the material [66, 67]. This ratio is often described by the dimensionless Föppl–von Kármán (*FvK*) number, $k_s {L_0}^2/k_b$, where k_s is the stretching stiffness, L_0 is an equilibrium edge length of linear spring in the mesh, and k_b is the bending stiffness. By following the same definition, we determine the range of the *FvK* number characterizing the budding region resulting in bud generation.

3.1.2. Bud emergence dependence on the Föppl–von Kármán number

Simulations with different *FvK* numbers were performed to test whether a bud can be generated (table 1). In this section, $\overline{\gamma} = 0.1$ and $\alpha_a = 0.1$ are fixed.

The simulations suggest that bud emergence depends on the *FvK* number. Bud emergence does not change if the *FvK* number remains the same while weight constants $\alpha_* \leqslant 1$. We will discuss scenarios where $\alpha_* > 1$ in section 4 and the supplemental information in more detail. Because the *FvK* number is the ratio of parameters representing level of stretching and bending, for the parameter values giving the same *FvK* number, the resulting deformations would be the same. Furthermore, this idea is used to reduce the number of parameter sets tested in our paper. Budding is more likely to occur with a sufficiently large *FvK* number, which can be achieved by either increasing the stretching stiffness or reducing the bending stiffness.

3.1.3. Bud emergence depends on critical elasticity

We first vary bending stiffness at the bud site using weight constant α_b, and the critical value, $\overline{\gamma}$, for equation (6), to study the effect on bud formation for cell surfaces with different fixed *FvK* numbers. Notice that according to the definition, larger α_b indicates stronger resistance of the cell surface to bending deformation. Nine simulations were performed for most of the parameter sets $(\alpha_b, \overline{\gamma})$. For each simulation, the outcome was counted as a bud emergence if a visible protrusion from the cell surface with a volume at least 5.5% of the total cell volume was generated. Otherwise, it was counted as a bud inhibition and indicated by 'no bud' (figure 6). Different values of α_b and $\overline{\gamma}$ were chosen as described in table S3. Simulation results indicate a clear cutoff value for bud emergence dependent on α_b and this cutoff reduces as $\overline{\gamma}$ increases, separating the parameter space into two different zones (figure 6(A)).

The effect of stochasticity is insignificant for parameter sets well within these two zones. However, for simulations with parameter sets near the boundary between these two zones, the effect of stochasticity involved in the cell wall remodeling becomes

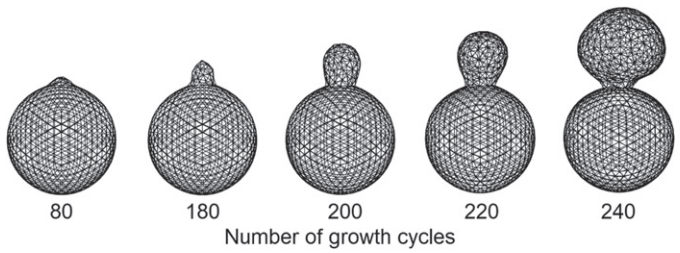

Figure 5. Sample simulation of bud formation under uniformly altered mechanical properties of the cell surface in the budding region after different numbers of growth cycles. After protrusion occurs, the growth of the bud starts as a tubule growth (left) then transitions to a more spherical expansion (right). The strong constraint from the chitin and septin rings we impose naturally restricts the cell surface expansion at the bud neck. Between successive growth cycles, the system is allowed to relax and have edge connections between nodes changed. The relaxation (iterative) step size is $\Delta t = 0.001$.

Table 1. Bud emergence for different *FvK* numbers.

α_s	α_b	*FvK* number	Bud emergence
0.2	0.02	3.624	Yes
0.75	0.075	3.624	Yes
0.2	0.05	1.450	No
0.4	0.1	1.450	No

more significant (figure 6(C)). In particular, with the parameters chosen near the boundary, budding can occur but not in every single trial.

Next, simulations were performed with fixed α_a and α_b, and perturbed α_s and $\overline{\gamma}$. A cutoff value, α_s, for bud emergence was also observed for each value of $\overline{\gamma}$ and this cutoff value increases as $\overline{\gamma}$ increases (figure 6(B)). This is expected because bud emergence depends on the physical properties described by the *FvK* number. The same ratio can be achieved by increasing the stretching stiffness or reducing the bending stiffness, while fixing the other.

3.1.4. Impact of the Föppl–von Kármán number on bud shape

In this section we investigate how different ratios of stretching and bending stiffness affect the bud shape. Since increasing the stretching stiffness is equivalent to reducing the bending stiffness when changing the Föppl–von Kármán number, in this section we fix α_s, α_a and vary both α_b and $\overline{\gamma}$. To evaluate the sphericity of the bud, we define $\Omega(\alpha_b, \overline{\gamma})$ as the distances between the cell surface nodes within the bud area to the center of the bud, for given α_b and $\overline{\gamma}$ that can generate a bud. Here the bud center is determined by the average of the *x*-, *y*-, and *z*-coordinate of all nodes in the bud region. Therefore, smaller range of $\Omega(\alpha_b, \overline{\gamma})$ indicates more spherical shape and the average of $\Omega(\alpha_b, \overline{\gamma})$ represents the radius of the sphere that fits the bud. We observe that the range of $\Omega(\alpha_b, \overline{\gamma})$ becomes smaller as the weight α_b applied to the bending modulus of the bud increases for $\overline{\gamma} = 0.05$ (figure 7). For different $\overline{\gamma}$ values, we observe the same trend regarding the deviation of $\Omega(\alpha_b, \overline{\gamma})$ versus α_b (table S4). This behavior is expected, as higher α_b leads to stronger resistance to bending deformation at the bud site and therefore more spherical shape can be maintained. We also expect more spherical shapes can be obtained when reducing the stretching modulus.

Taken together, results in this section suggest a tradeoff based on *FvK* numbers for any fixed critical value for γ, i.e. the dimensionless stretching-to-bending ratio must be sufficiently high at the bud site to generate a bud, while a higher ratio leads to less spherical bud shapes. Therefore, the ratio of stretching to bending moduli must be appropriately tuned by the polarizing molecules to give rise to buds with spherical shapes as observed in experiments.

3.2. Role of the stiffness of the budding neck in bud formation

It has been shown in experiments that chitin and septin rings assemblies are important in determining budding neck shape and other growth related activities during a cell cycle [21]. In wild type yeast budding, the bud neck is roughly 1.0 μm in diameter [19], while mutants with impaired chitin and septin rings can exhibit bud necks with approximately 2.68 μm in diameter.

It has also been shown that the septin based rings structure acts as a diffusion barrier to the polarity factors including Cdc42 and cortical proteins, and further affects the bud shape [68]. Here we investigate the mechanical contribution of the chitin and septin rings to bud formation, as well as the shape and size of the bud neck.

Different levels of the rigidity of the combined chitin and septin rings, modeled as an elastic rings with different linear spring coefficients, k_s^{ring}, are tested and the bud neck diameter is approximated from each simulation (figure 8(A)). Consistent with

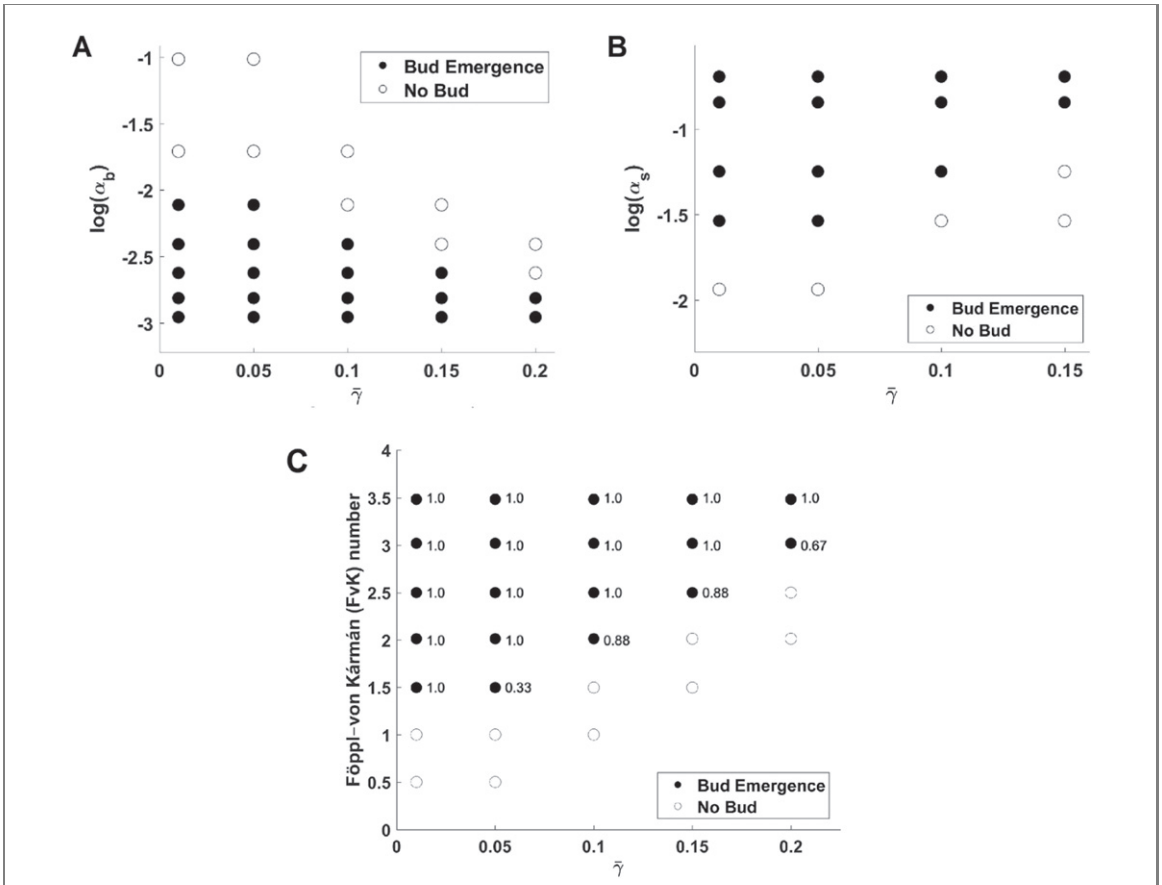

Figure 6. Diagrams describing the influence of $\overline{\gamma}$ on bud emergence. (A) Variation of bending stiffness (α_b) with fixed α_s and α_a. (B) Variation of stretching stiffness (α_s) with fixed α_b and α_a. Both plots show that budding can occur when increasing Föppl–von Kármán (*FvK*) number (dimensionless stretch-bend ratio) over a certain cutoff value, i.e., reducing α_b or increasing α_s. (C) Plot of combinations of *FvK* numbers and the normalized target expansion strain $\overline{\gamma}$ leading to bud emergence or lack of bud emergence. *FvK* numbers shown in (C) are the same as in (A) and (B). The number next to each data point indicates the percentage of simulations leading to bud emergence in the nine simulations run for corresponding *FvK* number.

experiments, a direct effect of the decreased constraint of the chitin and septin rings in the simulations is the widened budding neck. More precisely, we observe a sharp decay in the approximated budding neck diameter as k_s^{ring} increases (figure 8(A)).

Moreover, the standard deviation (SD) of the bud radii does not significantly depend on k_s^{ring}, ranging between 0.093 and 0.114, indicating that the rigidity of the chitin and septin rings does not impact the bud shape once budding occurs (figures 8(B)–(D)). In addition, increase in k_s^{ring} can slow down bud growth, or even prevent budding when the *FvK* number is not sufficiently high, as discussed in **SI.2**.

To summarize, in addition to preventing the diffusion of polarity molecules involved in the budding process, the rigid chitin and septin rings impact bud emergence and determine the neck shape without changing the bud shape. The bud neck width reduces as the rings stiffness increases and high rigidity may prevent bud formation.

3.3. Bud formation under different polarization patterns

Cdc42 orients actin cables to recruit more Cdc42 as well as new cell membrane and cell wall materials before bud formation. The mechanical properties at the bud site are regulated while the polarization of Cdc42 is established. Budding can start before Cdc42 obtains sharp polarity. In this section, instead of assuming the mechanical properties are regulated by Cdc42 with a steep polarized distribution and using the constant weights ($\alpha_s, \alpha_b, \alpha_a$) at the bud site, we allow the mechanical properties to undergo a smooth monotonic change from the mother cell to the bud region, which are altered most at the apical tip of the bud site, and study the corresponding conditions for bud emergence and the effect on bud shape.

In particular, we apply Hill functions to model the changes in mechanical properties due to the concentrated Cdc42 along the cell membrane near the bud site, as described in the supplemental information (**SI.3**). All weight functions have maximum value 1.0 in the mother cell, indicating no change in mechanical properties, and the minimum are set to be 0.5 for α_s, 0.052 for α_b, 0.1 for α_a at the bud tip, and $\overline{\gamma} = 0.05$. Different Hill coefficients n are adopted to model different polarization patterns. Larger n indicates a more concentrated change, i.e. the weight functions converge to the constant weights in the previous section as n approaches to infinity. We test $n = 8, 17, 35, 70$

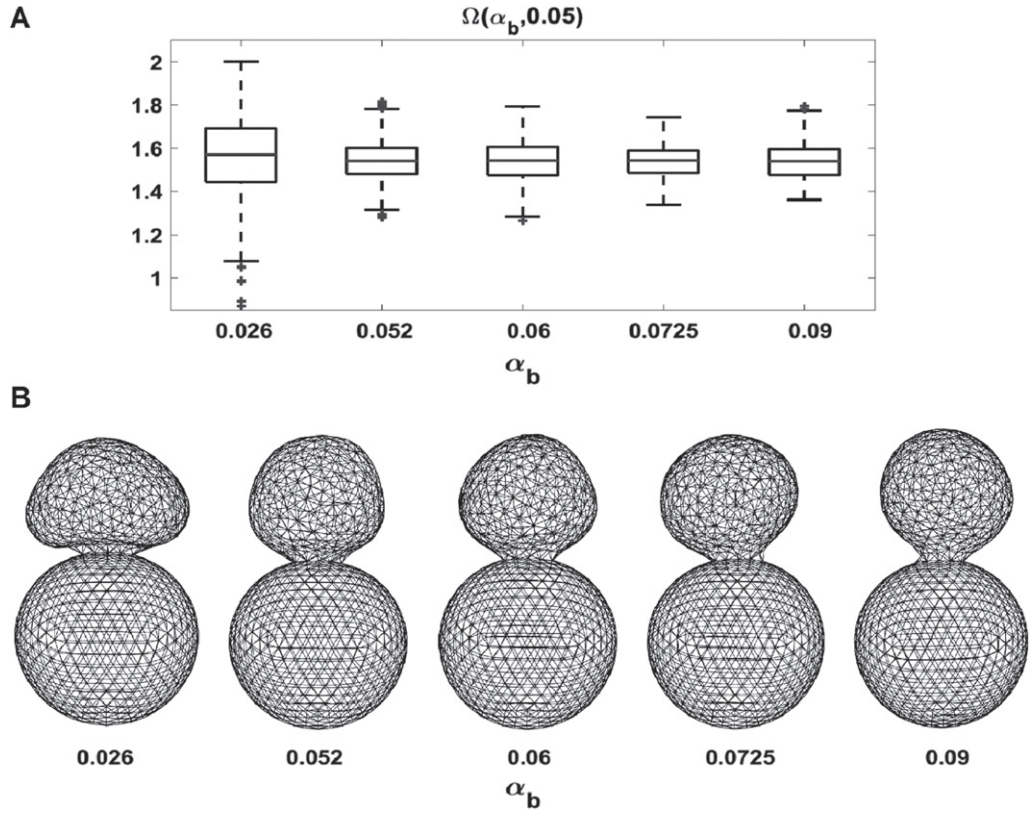

Figure 7. (A) Boxplot of the bud radii, $\Omega(\alpha_b, 0.05)$, for different α_b. As α_b increases, the budding region becomes more resistance to bending deformation and maintains better roundness in shape, hence leading to smaller SD of $\Omega(\alpha_b, 0.05)$. (B) A sample sequence of simulation snapshots for increasing values of α_b.

to ensure the shapes of the corresponding weight functions are distinguishable in terms of sharpness (figure 9(A)).

We found that, for $n = 8$, the cell cannot bud. For $n = 17$, a bud successfully emerges but exhibits a much narrower hourglass-shaped neck with an approximate diameter of 0.4–0.552 μm (figure 9(D)). For $n = 35$, two different types of budding in terms of the neck shape are observed in simulations: narrower and non-axisymmetric neck (figure 9(C1)), and similar neck shape as the constant weight cases (figure 9(C2)). The non-axisymmetric neck shape occurs more frequently in simulations, and the neck diameter ranges 0.87–1.005 μm approximately, which is calculated via the average of the max and min diameters in this case. For $n = 70$, budding can occur in a similar way as was observed when the weights were constant (figure 9(B)), which is expected for large n. Moreover the resulting neck diameter was approximately 1.087–1.14 μm, which is similar to experimental observations.

Overall, the simulations suggest that budding emergence depends on the concentration distribution of the mechanical regulating molecules. The change in the mechanical properties at the bud site controlled by a more polarized signaling molecule is more likely to generate a bud with more robustness in the bud shape. The bud neck obtained with less polarized weight functions becomes narrower and non-axisymmetric.

3.4. Bud formation under dynamic change in mechanical properties

Experiments show that Cdc42 polarizes at the apical tip region before bud formation and this highly concentrated distribution is maintained at the early stage of bud growth. As bud formation takes place, Cdc42 aggregates to reach a homogeneous distribution within the bud site [6]. Before cell division, Cdc42 is redirected from the bud cortex to the bud neck. This suggests that regulation of the mechanical properties might change temporally with strongest effect before bud formation or right after the apical protrusion. Therefore, we test a temporal restoration of altered mechanical properties at the bud site in our model to see whether the strong mechanical regulation, if only present in a short period at the beginning of the budding process, is sufficient or not.

3.4.1. Temporal restoration functions

Due to the energy dissipation approach used for mechanical relaxation in our simulations, the temporal restoration of the bud mechanical properties is assumed to be cell volume based, i.e., the evolution in time of the weights in altering mechanical potentials at the bud site is assumed to be linearly increasing with respect to the volume:

$$\alpha_{(i,V)}k_i = \alpha_{(i,0)}k_i + (\alpha_{(i,V')}k_i - \alpha_{(i,V_0)}k_i)(V - V_0)/ \times (V_m - V_0), \quad i \in \{s, b, a\}. \tag{8}$$

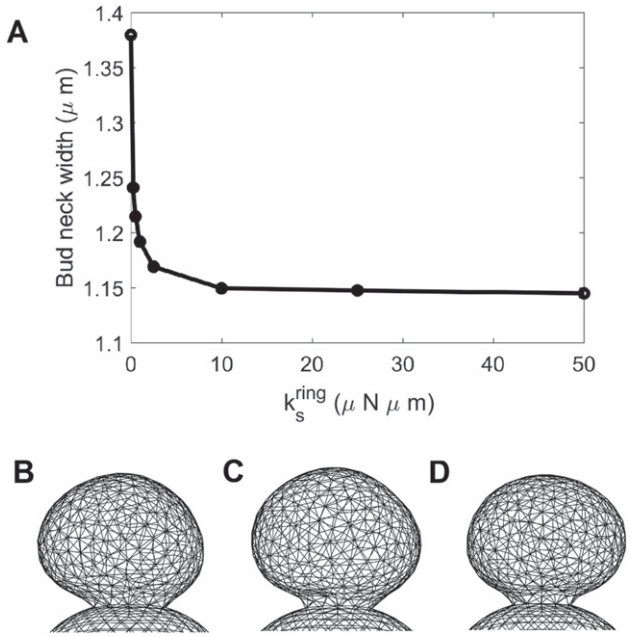

Figure 8. (A) The approximated diameter of the bud neck plotted against stiffness of the rings $k_s^{ring} = 0, 0.25, 0.5, 1, 2.5, 10, 25, 50$. A sharp decay is observed when $k_s^{ring}$is small. (B)–(D) Comparison of the bud shape and budding neck with $(\alpha_s, \alpha_b, \alpha_a) = (0.5, 0.06, 0.1)$ fixed and different rigidities of the chitin and septin rings. (B) $k_s^{ring} = 0.0$, (C) $k_s^{ring} = 0.25$, (D) $k_s^{ring} = 1.0$. The corresponding approximated SDs are 0.1135, 0.0980, 0.1113 respectively, which are close to the SD 0.0930 with $k_s^{ring} = 50.0$.

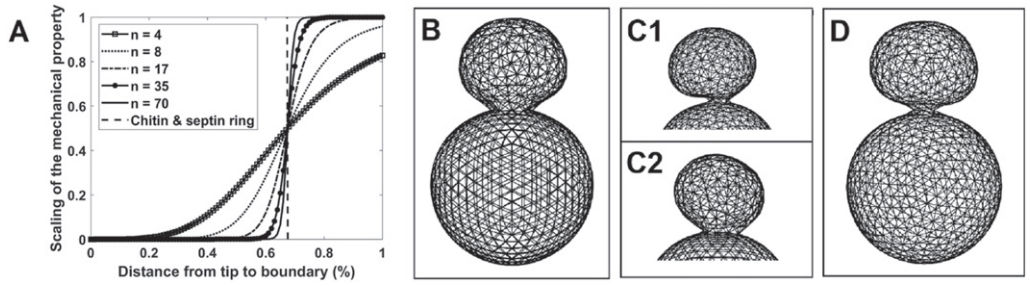

Figure 9. (A) Hill functions with different Hill coefficients used for spatially dependent changes in mechanical properties at the bud site. The Hill coefficients are chosen to be $n = 8, 17, 35, 70$. The weight represents level of the change, with being altered most at distance 0.0 and unaltered at distance 1.0. (B)–(D) Sample budding shapes based on different Hill coefficients. (B) $n = 70$, (C1), (C2) $n = 35$, (D) $n = 17$. Two different shapes of the budding neck are observed for $n = 35$: non-axisymmetric bud neck (C1) and axisymmetric bud neck (C2). Between these two modes, the non-axisymmetric bud neck appears more frequently in simulations.

Here $\alpha_{(i,V)}$ represents the weight applied to the linear spring potential (k_s), cosine bending potential (k_b), or the area expansion resistance (k_a), based on the current volume V. When the volume reaches the target volume V_m, the mechanical properties of the bud become identical to those of the mother cell. Here, V_0 represents the initial volume of the cell.

3.4.2. Temporal restoration of bud mechanical properties leads to symmetric bud shape

To test different restoration speeds from the altered state, we change the value of V_m. For example, the mechanical properties at the bud site will be fully restored to the same level as the mother cell when the cell volume doubles, i.e. $V_m = 2V_0$.

Similarly, setting $V_m = 1.5V_0$ and $V_m = 3V_0$ lead to expedited and delayed restoration compared to $V_m = 2V_0$, respectively. Based on the results of model calibration, we test the following parameter set as the altered state: $(\alpha_{s,V_0}, \alpha_{b,V_0}, \alpha_{a,V_0}, \overline{\gamma}) = (0.5, 0.0151, 0.1, 0.05)$. In simulations, the weights $\alpha_s, \alpha_b, \alpha_a$ are changed in time following equation (8). We found that temporal restoration of the mechanical properties leads to bud formation with more spherical and symmetric shapes (figure S3). Regardless of different choices of the restoration speed, improved bud roundness was observed once the bud formed (figure 10(A)). Namely, we compared the local SDs between buds satisfying total cell volume lies within $1.39V_0 - 1.45V_0$. Among these simulations, we choose those with a parameter set

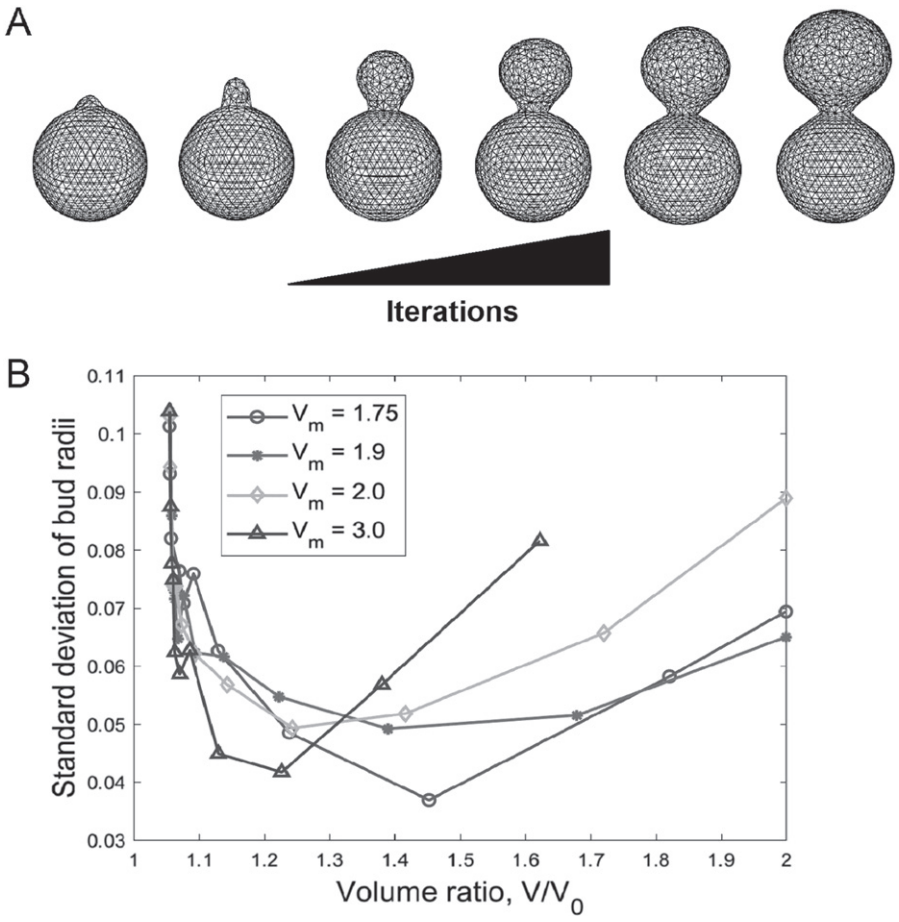

Figure 10. (A) Sample simulation of bud formation under temporal restoration of the cell surface mechanical properties in the budding region. After protrusion occurs, the growth of the bud starts as a tubule growth (left) then transitions to a more spherical expansion (right) compared to the simulation with time-independent changes in mechanical properties (figure 5). In this example, $V_m = 2V_0$. (B) SD of bud radii vs volume ratio V/V_0. The initially high SD corresponds to the tubule growth at the earliest stage of budding. The SD gradually decreases as the bud attains a more spherical shape. Higher target volume, V_m, implies slower restoration speed. The difference in restoration speed also affects how fast the bud growth transitions from apical (tubule) growth to isotropic growth, which later transitions into asymmetric growth as observed in the time-independent change in mechanical properties cases (i.e. fixed mechanical properties for budding region).

Table 2. Optimal standard deviation (SD) of the bud for uniformly altered and restorative mechanical properties. The SDs here are the lowest value obtainable from simulations. For rows with α_b, the values are extracted from data used in the supplemental information, table S4. Overall, the local SD of the bud using restorative mechanical properties is lower compared to the uniformly altered mechanical properties cases.

	Optimal overall SD	SD_u	SD_l	SD_n
$\alpha_b = 0.052$	0.0630	0.0490	0.0663	0.0602
$\alpha_b = 0.06$	0.0850	0.0766	0.0824	0.0836
$\alpha_b = 0.09$	0.0707	0.0707	0.0630	0.0671
$\alpha_b = 0.121$	0.0514	0.0409	0.0596	0.0425
$V_m = 2.0V_0$	0.0415	0.0368	0.0455	0.0350
$V_m = 3.0V_0$	0.0568	0.0544	0.0577	0.0552
$V_m = 1.75V_0$	0.0369	0.0282	0.0438	0.0268

containing $\overline{\gamma} = 0.05$ and $\alpha_s = 0.5$. Aside from the overall SD calculated over the whole bud, the local SD is selected to make a more detailed comparison. These SDs are quantified by using the upper hemisphere of the bud, denoted SD_u, lower hemisphere of the bud, denoted SD_l, and SD of the bud excluding the budding neck, SD_n. SD_u is calculated using cell surface nodes positioned above the center of the bud. SD_l is calculated using cell surface nodes positioned between the bud neck and the center of the bud. SD_n is calculated by considering only nodes whose z-coordinates are in the upper 90% of the height of the bud. The optimal values among simulations, based on SD_n, are presented in table 2.

In addition, we observed that the restoration speed had a significant impact on bud formation, as faster restoration led to bud inhibition, such as $V_m = 1.5V_0$. On the other hand, when the restoration speed was slower, such as $V_m = 3.0V_0$, the simulation showed asymmetric growth.

As the growth of the bud always starts with a tubule, the SD is higher at the early stage. Afterward, the bud growth becomes more isotropic, and the SD reduces. After that, asymmetric expansion leads to an increasing SD at the late stage of the simulation. Therefore, the overall curve of the SD shows nonlinearity. The speed of restoration also affects the SD. More specifically, slow restoration results in fast transition from tubule growth (high SD) to isotropic growth (low SD). In addition, slow restoration also leads to high SD during the late stage of simulation.

For $V_m = 3V_0$, the bud is initially generated in a spherical shape. Due to the slow restoration of mechanical properties allowing efficient expansion of the bud, the bud shape gradually becomes more ellipsoidal, thereby achieving a SD of bud radii similar to which is observed under time-independent changes in mechanical properties (table S4). This suggests a well-coordinated restoration of the bud mechanical properties may be necessary for symmetry maintenance of the bud. For $V_m = 2V_0$, a more symmetric bud shape is maintained after protrusion in comparison with the time-independent cases presented in section 3.1 (figure 10).

4. Discussion and conclusions

In this paper, a novel 3D coarse-grained particle-based model of a single cell is introduced and used to investigate the role of local changes in cell surface mechanical properties during early stages of yeast budding. The model combines nonhomogeneous representation of the cell surface with stiff rings structure to study cell growth and budding. It is calibrated using experimentally measured Young's modulus of the budding yeast cell wall [43]. The novelty of this modeling study lies in testing the main hypothesised mechanism of cell budding combining changing mechanical properties of the budding region with the impact from the constraint of chitin and septin rings.

Role of the change in mechanical properties. Model simulations supported the hypothesis that the bud cannot emerge unless the mechanical properties are weakened in the bud region. We also demonstrated that in the case of the bud region being as rigid as, or even more rigid than the mother cell at the early stage of budding, budding either fails to occur or occurs with a highly unbiological shape (figure S4). By assuming mechanical properties being weakened uniformly at the bud site by the polarized molecules, bud emergence was shown to depend on the Föppl–von Kármán (*FvK*) number (dimensionless ratio between stretching and bending moduli). Computationally when the velocity of adding new cell wall materials is reduced by increasing the target strain for area expansion, $\overline{\gamma}$, bud formation requires a higher *FvK* number when weakening the cell surface of the bud.

Growth and maintenance of the shape of the bud. For an emerging bud, symmetrical shape is biologically important because it indicates the balance between the composition and integrity of the bud surface, which is observed in wild type yeast budding. The sphericity of the bud shape, described via SD of the bud radii, was shown to be lower for: (1) comparatively less weakened bud cell surface characterized by lower *FvK* numbers or (2) reduced rate of cell surface material insertion characterized by the increase in critical value of γ (equation (6)). It is known that the chitin and septin rings serve as diffusion barriers for polarity factors at the early stage of budding. By using a computational model, we found that the resistance provided by the stiff rings prevents or slows bud growth. We also showed that neck diameter reduces as the stiffness increases, without affecting the bud shape. Also, by testing bud mechanical properties being altered by polarizing molecules with different distributions at the bud site throughout the duration of the budding process, it was shown that a cell was more likely to generate a bud with a more symmetric shape under a more polarized distribution. The bud neck obtained with less polarized distributions was narrower and non-axisymmetric.

Role of the temporal change in bud mechanical properties. By incorporating a dynamical restoration of weakened bud mechanical properties to the level of the mother cell at the bud site, the resulting bud shape was shown to be more symmetric and spherical, as compared with the ones with fixed mechanical properties. Fast restoration was shown to prevent bud formation and slow restoration to lead to development of an asymmetric bud.

Computational implementation of the model. In this study, the triangular mesh was used to directly model mechanical properties of a budding yeast cell. This is different from another more traditional approach where the triangular mesh is used as the discretization technique to approximate solutions to partial differential equations. In our mechanical model, by using parameters scaled with specific mesh size in energy functions, all the mechanical properties remain the same and the simulation results under different conditions should not be affected by the mesh size [59]. To verify that simulation outcomes are independent of the mesh size, we have tested our model on a refined mesh, which initially consists of 5120 triangles, and obtained the same conclusions as those obtained on the coarser mesh (**SI.6**). In order to achieve both accuracy and efficiency of the numerical

simulations, we used a coarser mesh with 1280 triangles as the initial condition for all simulations in the paper.

Model calibration. So far the model was calibrated based on the mechanical properties of the mother cell, final bud neck size and bud shape. An example of the calibration of the time scale under the assumption that the bud surface area increases linearly in time [69] is provided in **SI.7**. We also intend to calibrate the time scale in future using more precise and consistent experimental data such as velocities of emerging buds, when it becomes available. Notice that model simulations show that different mechanical properties of the bud region give rise to different velocities of bud growth. We hope that our model predictions might motivate experimentalists to conduct measurements of bud mechanical properties, e.g. AFM measurements, during bud initiation. Once the time series of experimental measurements becomes available, our model can be calibrated to replace relaxation time step by biologically realistic time. (The proposed time step calibration approach is presented in **SI.7**).

Testable predictions and suggested experiments. Our model simulation results also predict that budding can occur only if the bud region becomes less rigid and easier to bend at the early stage, which might be due to the degradation of cell wall components. To test this prediction, experiments can be carried out to measure the mechanical properties of the bud region during the initiation of budding. The underlying mechanism can be further investigated by applying cell wall degrading enzymes to a normal yeast cell and measuring the consequent mechanical change in the cell wall β-glucan network. Biologically a bud should eventually achieve surface elasticity comparable to the mother cell, otherwise multiple rounds of reproduction will lead to defective cells with a highly weakened cell surface. To verify that, experimental measurements of the mechanical properties of the bud region at different stages of budding are needed. Coincidentally, the polarization signal Cdc42 loses its polarized state after some time during the budding process. A time series of measurements of the surface elasticity and the Cdc42 distribution could confirm predictions of the temporal change on the bud mechanical properties obtained by our model.

Future directions. Although calibrated by using data for budding yeast, our 3D model can be applied to study cell growth and budding in other biological systems. It allows one to study the effect of local regulation of mechanical properties leading to global morphological changes. For instance, investigating how adverse effects due to local perturbations in the mechanical properties can propagate during growth is important for getting a better understanding of morphogenesis. In future, we plan to include in the modeling approach dynamic biochemical signaling networks submodel coupled with the cellular and subcellular mechanical submodels.

Namely, to investigate the regulation of the mechanical properties more precisely, it is worthwhile to include the model of spatiotemporal dynamics of the signaling molecules. The triangular mesh used for the mechanical model, with re-meshing techniques implemented to improve the element regularity, would be used to simulate diffusion-reaction systems of equations describing biochemical signals. Several studies have already studied the connection between biochemical signaling and cell mechanics in mating yeast and tubule formation [42, 70, 71]. However, understanding of the coupling between the biochemical signaling pathways and cell mechanics for the yeast budding process is still incomplete. A biologically calibrated mechano-chemical model would be helpful providing predictions to be tested in future experiments.

The model described in this paper oversimplifies contributions from cytosol components of the cell including nucleus, vacuole and actin-filaments. At the same time, the actin-filaments play a very significant role in cell surface expansion [72–74]. The nucleus also plays an important role especially in G2 and M phases of the cell cycle [75]. Recently our group developed a more refined 2D mechanical SCE type model with detailed description of the nucleus, actomyosin and cadherin, to study tissue bending mechanisms in a wing of a Drosophila embryo [76]. We are now working on incorporating these new components as well as biochemical submodel into our 3D model of an asymmetric cell growth which can be also used for studying viral budding and other vegetative reproduction processes performed via budding.

Acknowledgments

The authors acknowledge partial support from the National Science Foundation Grant DMS-1762063 through the joint NSF DMS/NIH NIGMS Initiative to Support Research at the Interface of the Biological and Mathematical Sciences and National Science Foundation Grants DMS-1853701 and DMS 2029814. RZ was supported by the National Science Foundation through Grant DMR-1719550. Simulations were performed using the resources of the HPCC at University of California, Riverside.

ORCID iDs

Kevin Tsai https://orcid.org/0000-0003-0312-9144
Ali Nematbakhsh https://orcid.org/0000-0001-7411-6039
Weitao Chen https://orcid.org/0000-0003-3362-5982
Mark Alber https://orcid.org/0000-0002-7153-1138

References

[1] Drubin D G 1991 Development of cell polarity in budding yeast *Cell* **65** 1093–6
[2] Li R and Murray A W 1991 Feedback control of mitosis in budding yeast *Cell* **66** 519–31
[3] Zhang X, Bi E, Novick P, Du L, Kozminski K G, Lipschutz J H and Guo W 2001 Cdc42 interacts with the exocyst and regulates polarized secretion *J. Biol. Chem.* **276** 46745–50
[4] Hao N 2006 *The Analysis of Feedback Regulation in Yeast Signal Transduction Pathways* Doctoral dissertation (Chapel Hill, NC: University of North Carolina at Chapel Hill)
[5] Kaeberlein M 2010 Lessons on longevity from budding yeast *Nature* **464** 513–9
[6] Bi E and Park H-O 2012 Cell polarization and cytokinesis in budding yeast *Genetics* **191** 347–87
[7] Geymonat M and Segal M 2017 Intrinsic and extrinsic determinants linking spindle pole fate, spindle polarity, and asymmetric cell division in the budding yeast S. cerevisiae *Results Probl. Cell Differ.* **61** 49–82
[8] Litsios A *et al* 2019 Differential scaling between G1 protein production and cell size dynamics promotes commitment to the cell division cycle in budding yeast *Nat. Cell Biol.* **21** 1382–92
[9] Kollár R, Reinhold B B, Petráková E, Yeh H J C, Ashwell G, Drgonová J, Kapteyn J C and Klis F Mand Cabib E 1997 Architecture of the yeast cell wall *J. Biol. Chem.* **272** 17762–75
[10] Hanschke R and Schauer F 1996 Improved ultrastructural preservation of yeast cells for scanning electron microscopy *J. Microsc.* **184** 81–7
[11] Hapala I, Griač P, Nosek J, Sychrová H and Tomáška Ľ 2013 Yeast membranes and cell wall: from basics to applications *Curr. Genet.* **59** 167–9
[12] Heun P, Laroche T, Raghuraman M K and Gasser S M 2001 The positioning and dynamics of origins of replication in the budding yeast nucleus *J. Cell Biol.* **152** 385–400
[13] Chiou J-g, Balasubramanian M K and Lew D J 2017 Cell polarity in yeast *Annu. Rev. Cell Dev. Biol.* **33** 77–101
[14] Lai H, Chiou J-G, Zhurikhina A, Zyla T R, Tsygankov D and Lew D J 2018 Temporal regulation of morphogenetic events in Saccharomyces cerevisiae *Mol. Biol. Cell* **29** 2069–83
[15] Caviston J P, Tcheperegine S E and Bi E 2002 Singularity in budding: a role for the evolutionarily conserved small GTPase Cdc42p *Proc. Natl Acad. Sci.* **99** 12185–90
[16] Lesage G and Bussey H 2006 Cell wall assembly in Saccharomyces cerevisiae *Microbiol. Mol. Biol. Rev.* **70** 317–43
[17] Cabib E and Arroyo J 2013 How carbohydrates sculpt cells: chemical control of morphogenesis in the yeast cell wall *Nat. Rev. Microbiol.* **11** 648–55
[18] Schmidt M, Varma A, Drgon T, Bowers B and Cabib E 2003 Septins, under Cla4p regulation, and the chitin rings are required for neck integrity in budding yeast *Mol. Biol. Cell* **14** 2128–41
[19] Blanco N, Reidy M, Arroyo J and Cabib E 2012 Crosslinks in the cell wall of budding yeast control morphogenesis at the mother-bud neck *J. Cell Sci.* **125** 5781–9
[20] Gladfelter A S, Bose I, Zyla T R, Bardes E S G and Lew D J 2002 Septin rings assembly involves cycles of GTP loading and hydrolysis by Cdc42p *J. Cell Biol.* **156** 315–26
[21] Gladfelter A S, Kozubowski L, Zyla T R and Lew D J 2005 Interplay between septin organization, cell cycle and cell shape in yeast *J. Cell Sci.* **118** 1617–28
[22] McMurray M A, Bertin A, Garcia G 3rd, Lam L, Nogales E and Thorner J 2011 Septin filament formation is essential in budding yeast *Dev. Cell* **20** 540–9
[23] De I M, Marechal P-A and Gervais P 1996 Passive response of Saccharomyces cerevisiaeto osmotic shifts: cell volume variations depending on the physiological state *Biochem. Biophys. Res. Commun.* **227** 519–23
[24] Schaber J *et al* 2010 Biophysical properties of Saccharomyces cerevisiae and their relationship with HOG pathway activation *Eur. Biophys. J.* **39** 1547–56
[25] Proctor S A, Minc N, Boudaoud A and Chang F 2012 Contributions of turgor pressure, the contractile rings, and septum assembly to forces in cytokinesis in fission yeast *Curr. Biol.* **22** 1601–8
[26] Goldenbogen B, Giese W, Hemmen M, Uhlendorf J, Herrmann A and Klipp E 2016 Dynamics of cell wall elasticity pattern shapes the cell during yeast mating morphogenesis *Open Biol.* **6** 160136
[27] Park H-O and Bi E 2007 Central roles of small GTPases in the development of cell polarity in yeast and beyond *Microbiol. Mol. Biol. Rev.* **71** 48–96
[28] Smith J A, Hall A E and Rose M D 2017 Membrane curvature directs the localization of Cdc42p to novel foci required for cell–cell fusion *J. Cell Biol.* **216** 3971–80
[29] Hall A E and Rose M D 2019 Cell fusion in yeast is negatively regulated by components of the cell wall integrity pathway *Mol. Biol. Cell* **30** 441–52
[30] Altenburg T, Goldenbogen B, Uhlendorf J and Klipp E 2019 Osmolyte homeostasis controls single-cell growth rate and maximum cell size of Saccharomyces cerevisiae *NPJ Syst. Biol. Appl.* **5** 34
[31] Klis F M, Boorsma A and De Groot P W J 2006 Cell wall construction in Saccharomyces cerevisiae *Yeast* **23** 185–202
[32] Deng H, Dutta P and Liu J 2018 Stochastic simulations of nanoparticle internalization through transferrin receptor dependent clathrin-mediated endocytosis *Biochim. Biophys. Acta Gen. Subj.* **1862** 2104–11
[33] Kaksonen M and Roux A 2018 Mechanisms of clathrin-mediated endocytosis *Nat. Rev. Mol. Cell Biol.* **19** 313–26
[34] Ruiz-Herrero T, Velasco E and Hagan M F 2012 Mechanisms of budding of nanoscale particles through lipid bilayers *J. Phys. Chem.* B **116** 9595–603
[35] Bahrami A H, Raatz M, Agudo-Canalejo J, Michel R, Curtis E M, Hall C K, Gradzielski M, Lipowsky R and Weikl T R 2014 Wrapping of nanoparticles by membranes *Adv. Colloid Interface Sci.* **208** 214–24
[36] Raatz M, Lipowsky R and Weikl T R 2014 Cooperative wrapping of nanoparticles by membrane tubes *Soft Matter* **10** 3570–7
[37] Gompper G and Kroll D M 1996 Random surface discretizations and the renormalization of the bending rigidity *J. Phys.* I **6** 1305–20
[38] Gompper G and Kroll D M 1998 Membranes with fluctuating topology: Monte Carlo simulations *Phys. Rev. Lett.* **81** 2284–7
[39] Kohyama T, Kroll D M and Gompper G 2003 Budding of crystalline domains in fluid membranes *Phys. Rev.* E **68** 061905
[40] Okuda S and Eiraku M 2017 Role of molecular turnover in dynamic deformation of a three-dimensional cellular membrane *Biomech. Model. Mechanobiol.* **16** 1805–18
[41] Banavar S P, Gomez C, Trogdon M, Petzold L R, Yi T-M and Campàs O 2018 Mechanical feedback coordinates cell wall expansion and assembly in yeast mating morphogenesis *PLoS Comput. Biol.* **14** e1005940
[42] Campàs O and Mahadevan L 2009 Shape and dynamics of tip-growing cells *Curr. Biol.* **19** 2102–7
[43] Dague E, Bitar R, Ranchon H, Durand F, Yken H M and François J M 2010 An atomic force microscopy analysis of yeast mutants defective in cell wall architecture *Yeast* **27** 673–84
[44] de Becze G I 1956 Yeasts *Appl. Microbiol.* **4** 1–12
[45] Sherman F 2002 *Getting Started with Yeast Methods in Enzymology* vol 350 ed C Guthrie and G R Fink (New York: Academic) pp 3–41

[46] Li S, Roy P, Travesset A and Zandi R 2018 Why large icosahedral viruses need scaffolding proteins *Proc. Natl Acad. Sci. USA* **115** 10971–6
[47] Panahandeh S, Li S, Marichal L, Leite Rubim R, Tresset G and Zandi R 2020 How a virus circumvents energy barriers to form symmetric shells *ACS Nano* **14** 3170–80
[48] Chen H, Howell A S, Robeson A and Lew D J 2011 Dynamics of septin rings and collar formation in Saccharomyces cerevisiae *Biol. Chem.* **392** 689–97
[49] Glomb O and Gronemeyer T 2016 Septin organization and functions in budding yeast *Frontiers Cell Dev. Biol.* **4** 123
[50] Abeln S, Vendruscolo M, Dobson C M and Frenkel D 2014 A simple lattice model that captures protein folding, aggregation and amyloid formation *PLoS One* **9** e85185
[51] Panahandeh S, Li S and Zandi R 2018 The equilibrium structure of self-assembled protein nano-cages *Nanoscale* **10** 22802–9
[52] Luo Y, Wang J, Liu B, Wang Z, Yuan Y and Yue T 2015 Effect of yeast cell morphology, cell wall physical structure and chemical composition on patulin adsorption *PLoS One* **10** e0136045
[53] Hurtado-Guerrero R, Schüttelkopf A W, Mouyna I, Ibrahim A F M, Shepherd S, Fontaine T, Latgé J-P and van Aalten D M F 2009 Molecular mechanisms of yeast cell wall glucan remodeling *J. Biol. Chem.* **284** 8461–9
[54] Chen L iFEM https://www.math.uci.edu/~chenlong/programming.html
[55] Farhadifar R, Röper J-C, Aigouy B, Eaton S and Jülicher F 2007 The influence of cell mechanics, cell-cell interactions, and proliferation on epithelial packing *Curr. Biol.* **17** 2095–104
[56] Noguchi H and Gompper G 2005 Dynamics of fluid vesicles in shear flow: effect of membrane viscosity and thermal fluctuations *Phys. Rev.* E **72** 011901
[57] Noguchi H and Gompper G 2004 Fluid vesicles with viscous membranes in shear flow *Phys. Rev. Lett.* **93** 258102
[58] Fedosov D A, Lei H, Caswell B, Suresh S and Karniadakis G E 2011 Multiscale modeling of red blood cell mechanics and blood flow in malaria *PLoS Comput. Biol.* **7** e1002270
[59] Wagner J and Zandi R 2015 The robust assembly of small symmetric nanoshells *Biophys. J.* **109** 956–65
[60] Hicks S D and Henley C L 2006 Irreversible growth model for virus capsid assembly *Phys. Rev.* E **74** 031912
[61] Smith A E, Zhang Z and Thomas C R 2000 Wall material properties of yeast cells: Part 1. Cell measurements and compression experiments *Chem. Eng. Sci.* **55** 2031–41
[62] McKay M D, Beckman R J and Conover W J 1979 Comparison of three methods for selecting values of input variables in the analysis of output from a computer code *Technometrics* **21** 239–45
[63] Marino S, Hogue I B, Ray C J and Kirschner D E 2008 A methodology for performing global uncertainty and sensitivity analysis in systems biology *J. Theor. Biol.* **254** 178–96
[64] Goldman R N 1991 IV.1 - Area of planar polygons and volume of polyhedra. In Graphics gems II ed J Arvo (San Diego: Morgan Kaufmann) pp 170–1
[65] Wedlich-Soldner R, Altschuler S, Wu L and Li R 2003 Spontaneous cell polarization through actomyosin-based delivery of the Cdc42 GTPase *Science* **299** 1231–5
[66] Vetter R, Stoop N, Wittel F K and Herrmann H J 2014 Simulating thin sheets: buckling, wrinkling, folding and growth Journal of Physics: Conference Series **487** 012012
[67] Boltz H-H and Kierfeld J 2015 Shapes of sedimenting soft elastic capsules in a viscous fluid *Phys. Rev.* E **92** 033003
[68] Oh Y and Bi E 2011 Septin structure and function in yeast and beyond *Trends Cell Biol.* **21** 141–8
[69] Klis F M, de Koster C G and Brul S 2014 Cell wall-related bionumbers and bioestimates of Saccharomyces cerevisiae and Candida albicans *Eukaryot. Cell* **13** 2–9
[70] Chen W, Nie Q, Yi T-M and Chou C-S 2016 Modelling of yeast mating reveals robustness strategies for cell-cell interactions *PLoS Comput. Biol.* **12** e1004988
[71] Trogdon M, Drawert B, Gomez C, Banavar S P, Yi T-M, Campàs O and Petzold L R 2018 The effect of cell geometry on polarization in budding yeast *PLoS Comput. Biol.* **14** e1006241
[72] Moseley J B and Goode B L 2006 The yeast actin cytoskeleton: from cellular function to biochemical mechanism *Microbiol. Mol. Biol. Rev.* **70** 605–45
[73] Ayscough K R, Stryker J, Pokala N, Sanders M, Crews P and Drubin D G 1997 High rates of actin filament turnover in budding yeast and roles for actin in establishment and maintenance of cell polarity revealed using the actin inhibitor latrunculin-A *J. Cell Biol.* **137** 399–416
[74] Yang H-C and Pon L A 2002 Actin cable dynamics in budding yeast *Proc. Natl Acad. Sci.* **99** 751–6
[75] Howell A S and Lew D J 2012 Morphogenesis and the cell cycle *Genetics* **190** 51–77
[76] Nematbakhsh A, Levis M, Kumar N, Chen W, Zartman J and Alber M 2020 Epithelial organ shape is generated by patterned actomyosin contractility and maintained by the extracellular matrix PLoS Computational Biology 16(8):e1008105